

This is a list of commands provided by the L^AT_EX style file *L-AA*. For a complete description of these commands please refer to the user's guide.

The beginning of an article

```
\documentstyle{l-aa}
<macro definitions>
\begin{document}
\thesaurus{<section>(<thesaurus code>; ...
  <thesaurus code>)}
\title{<title of article>}
\subtitle{<subtitle of article>}
\author{<name of first author>\inst{<number>}
  \and <name of second author>\inst{<number>} ...}
\institute{<first address> \and <second address>}
\thanks{<text of footnote>}
\thanks{{\it Present address:\/} <address>}
\offprints{<name>}
\date{Received <date>; accepted <date>}
\maketitle
```

```
\maintitlerunninghead{<short title>}
\authorrunninghead{<names of authors> et al.}
```

Footnote mark separator \fnmsep

```
\begin{abstract}
<abstract>
\keywords{<keyword -- keyword -- ...>}
\end{abstract}
```

Headings

```
\section{title of section}
\subsection{title of subsection}
\subsubsection{title of subsection}
\paragraph{title of paragraph}
```

Special typefaces

```
{\em <text>}
\vec{<letter>}
\tens{<letter>}
{\sc <text>}
```

Footnotes

```
\footnote{<text>}
```

one column

```
\begin{figure}
\picplace{<height> cm}
\caption[]{<text>}
\end{figure}
```

two columns

```
\begin{figure*}
\picplace{<height> cm}
\caption[]{<text>}
\end{figure*}
```

Tables

one column

```
\begin{table}
\caption[]{<text>}
\begin{flushleft}
<input for table>
\end{flushleft}
\end{table}
```

two columns

```
\begin{table*}
\caption[]{<text>}
\begin{flushleft}
<input for table>
\end{flushleft}
\end{table*}
```

Acknowledgements

```
\begin{acknowledgements} <text>
\end{acknowledgements}
```

Appendices

```
\appendix
```

References

```
\cite{<ref-id>}
```

```
\begin{thebibliography}{}
\bibitem[<year>]{<ref-id>} <entry>
\bibitem[<year>]{<ref-id>} <entry>
...
\end{thebibliography}
```

Signs and characters

See user's guide

The end

```
\end{document}
```

Discovery of weak 6.7-GHz CH₃OH masers in a sample of high-mass Hi-GAL sources

L. Olmi^{1,2}, E. D. Araya³, P. Hofner⁴, S. Molinari⁵, J. Morales Ortiz², L. Moscadelli¹, and M. Pestalozzi⁵

¹ INAF, Osservatorio Astrofisico di Arcetri, Largo E. Fermi 5, I-50125 Firenze, Italy, e-mail: olmi.luca@gmail.com

² University of Puerto Rico, Rio Piedras Campus, Physics Dept., Box 23343, UPR station, San Juan, Puerto Rico, USA

³ Physics Department, Western Illinois University, 1 University Circle, Macomb, IL 61455, USA

⁴ New Mexico Institute of Mining and Technology, Physics Department, 801 Leroy Place, Socorro, NM 87801, USA. Adjunct Astronomer at the National Radio Astronomy Observatory.

⁵ Istituto di Fisica dello Spazio Interplanetario - INAF, via Fosso del Cavaliere 100, I-00133 Roma, Italy

Received; accepted

ABSTRACT

Context. Maser lines from different molecular species, including water, hydroxyl, and methanol, are common observational phenomena associated with massive star forming regions. In particular, since its discovery, the 6.7-GHz methanol maser has been recognized as one of the clearest signposts to the formation of young high-mass stars.

Aims. The methanol maser thus appears as an ideal tool to study the early phases of massive star formation. However, it is difficult to establish the exact start of the methanol maser phase, and it would then be interesting to detect and study low-flux density methanol masers (i.e., $\lesssim 0.1$ Jy or even $\ll 0.1$ Jy), in order to determine if they can effectively be used to mark a specific evolutionary phase in high-mass star formation.

Methods. Past surveys have been unable to systematically detect many low-flux density methanol masers, and thus we do not yet know how many such masers exist in the Galaxy and what is their physical nature. A large sample of massive cores can now be found in the Herschel infrared GALactic Plane Survey (Hi-GAL), which we have used to search for methanol and excited OH masers towards a sample of pre- and proto-stellar high-mass clumps using the Arecibo telescope.

Results. Out of a sample of 107 observed Hi-GAL sources we detected a total of 32 methanol masers, with 22 sources being new and weak (median peak flux density 0.07 Jy) detections, in the Galactic longitude range $[32^\circ.0, 59^\circ.8]$. We also detected 12 6.035-GHz OH maser, with 9 objects being new detections. Our survey covers a similar range of source distances as the “Arecibo Methanol Maser Galactic Plane Survey” (or AMGPS, Pandian et al. 2007), but the methanol masers detected by us are clearly shifted towards lower integrated flux densities.

Conclusions. The newly detected methanol masers are mostly of low-luminosity and, except for some sources, their weakness is not due to distance effects or positional offsets. No specific correlation is found with the physical parameters of the Hi-GAL clumps, except for sources with both CH₃OH and OH masers which tend to have higher mass and luminosity. The intensity of the methanol masers correlates well with the velocity range of the maser emission, which suggests that the low brightness of these masers is related to the number of maser spots in the emitting region and their evolution with time.

Key words. stars: formation – ISM: clouds – ISM: molecules

1. Introduction

Our current understanding of the formation process of intermediate to massive stars ($M \gtrsim 5M_\odot$) is limited, due to a combination of theoretical and observational challenges. On the theoretical side, the formation of massive stars is a highly complex process, which is also dependent on the interaction between the large-scale ($\gtrsim 10$ pc) structure of molecular clouds/clumps and dynamic fragmentation properties during the pre-stellar phase.

On the observational side, only very recently some progress has been made toward the identification and study of the earliest phases of high-mass star formation (HMSF), and the transition from the high-mass starless core (HMSC) phase (the likely precursors of massive stars and clusters), to the high-mass proto-stellar object phase. However, the physical conditions in the HMSC and the exact evolutionary path from HMSC to massive stars are not well constrained.

Maser lines from different molecular species, including water, hydroxyl, and methanol, are common observational phenomena associated with massive star forming regions. The relation

between different types of masers found around young stellar objects may yield important information about the evolutionary state of the regions (e.g., Szymczak & Gérard 2004, Breen et al. 2010). In particular, since its discovery (Menten 1991), the 6.7-GHz methanol maser has been recognized as one of the clearest signposts to the formation of young high-mass stars. Theoretical models (e.g., Cragg et al. 2002) and observational studies (e.g., Ellingsen 2006) suggest that methanol masers are exclusively associated with early phases of massive star formation. The methanol maser thus appears as an ideal tool to detect a short-lived phase of HMSF, between the end of the large scale accretion and the formation of massive proto-stars (Pestalozzi 2012). However, it is difficult to establish the exact start of the methanol maser phase and study the physical properties in that phase.

A large sample of massive cores can now be found in the *Herschel* infrared GALactic Plane Survey (Hi-GAL), a key program of the *Herschel* Space Observatory to carry out a 5-band photometric imaging survey at 70, 160, 250, 350, and 500 μm of a $|b| \leq 1^\circ$ -wide strip of the Milky Way Galactic plane

(Molinari et al. 2010). This survey is now providing us with large samples of dust clumps in a variety of evolutionary stages and in various star-forming environments.

2. Observations

2.1. Previous observations

During the last 10–15 years, extensive 6.7-GHz methanol maser searches have been undertaken using two different strategies: (1) targeted searches toward colour-selected infrared sources and known regions of star formation (e.g., Walsh et al. 1997, Szymczak et al. 2002); and, (2) unbiased surveys covering portions of the Galactic plane (for a summary see Green et al. 2009). In particular, the Methanol Multibeam Survey (MMBS, Green et al. 2009) when completed will cover the whole Galactic plane in longitude, and in a latitude range $|b| \leq 2^\circ$. This survey also covers a previous smaller survey carried out at Arecibo (the ‘‘Arecibo Methanol Maser Galactic Plane Survey’’, or AMGPS, Pandian et al. 2007, 2011). All of these surveys have detected a total of about 800 masers in the range $\ell = 20^\circ - 186^\circ$, but many more ($\sim 1200 - 2500$) are expected to be found (van der Walt 2005, Pestalozzi et al. 2007).

The targeted $1-\sigma$ noise level of the MMBS is ≤ 0.2 Jy (Green et al. 2008), whereas the AMGPS yielded an rms noise level of ~ 70 mJy (Pandian et al. 2007). These are similar to the deepest previous unbiased surveys which had $1-\sigma$ sensitivities between 0.09 Jy and 1 Jy (see Pestalozzi et al. 2005). Pandian & Goldsmith (2007) found that the peak of the distribution of methanol masers as a function of flux density occurred between 0.9 and 3 Jy. They also found a turnover in the number of sources at lower flux densities, but they could not determine the shape of the distribution due to their completeness limit of 0.27 Jy (the completeness limit in the MMBS is ≈ 0.8 Jy).

Therefore, these surveys have been unable to detect a significant number of *low-flux density* (i.e., $\lesssim 0.1$ Jy or even $\ll 0.1$ Jy) methanol masers, and thus we do not yet know how many such masers exist in the Galaxy and what is their physical nature. In particular, in light of the association of the 6.7-GHz methanol maser with the early stages of high-mass star formation (e.g., Pestalozzi et al. 2002), it would be interesting to analyze if low-flux density masers can effectively be used to mark a specific evolutionary phase in high-mass star formation.

2.2. Selection of the source sample

The Hi-GAL survey offers the best opportunity to further study the issues described above, since it allows us to look at large clump populations in various clouds with different physical conditions, while using a self-consistent analysis to derive their physical parameters (see, e.g., Elia et al. 2010, 2013, Olmi et al. 2013). Previous surveys suggest that methanol masers do not form towards low-mass molecular clumps. Therefore, the mass of the Hi-GAL clump can be used as the main selection parameter to help identify new methanol masers.

For our observations at Arecibo, which were divided in three sessions (July 2012, January 2013 and May 2013), we selected (and observed) a sample of 107 Hi-GAL sources using the following basic criteria: (i) the targets had to be located in the inner Galaxy accessible to Arecibo (we limited the range to $\ell \sim 30^\circ - 60^\circ$); (ii) the sources had a mass $M > 10 M_\odot$ (since the true distance to these Hi-GAL sources had not been estimated yet, their preliminary masses were calculated using an arbitrary distance of 1 kpc); (iii) the sources must have been detected in all

Hi-GAL bands longward of $70 \mu\text{m}$. (iv) for the sources observed during the January and May 2013 sessions we also checked that they were not near (within 1 arcmin radius) any of the already known methanol masers. Note that given the observing restrictions at Arecibo, our selection criteria intentionally used only mass as main parameter in order to have at our disposal a large enough sample of sources.

2.3. Arecibo observations

The observations were conducted with the 305 m Arecibo Telescope¹ in Puerto Rico, between July 2012 and May 2013 as we already mentioned. We used the C-Band High receiver to simultaneously observe the $(5_1 - 6_0)$ transition of A⁺ methanol at 6668.518-MHz and the 6035.092-MHz ($^2\Pi_{3/2} J = 5/2, F = 3 - 3$) excited-state OH maser line.

We used the WAPP spectrometer, full Stokes polarization setup, 3-level sampling, 6.25 MHz (280 km s^{-1}) bandwidth, and 4096 channels per polarization, resulting in a channel separation of 1.53 kHz (0.068 km s^{-1}). We observed in ON-source (total power) mode, with integration times of 5 minutes, which yielded a rms noise level of $\approx 5 - 10$ mJy in each spectral channel, depending on the smoothing level. Our sensitivity was thus much better than that achieved in the MMBS and AMGPS surveys. The center bandpass LSR velocity was set to 70 km s^{-1} . The calibrator B2128+048 was observed in every run for pointing and system checking (1 min on-source observations). The pointing was typically better than $10''$. We measured a telescope beam size of $\sim 42''$ (at 6.6 GHz), and a typical gain of $\sim 6 \text{ K Jy}^{-1}$.

Data reduction was done in IDL² using specialized reduction routines provided by the Arecibo Observatory. After checking for consistency we subtracted low-order polynomial baselines. The spectra were imported to CLASS³ to measure line parameters and for further analysis.

3. Results

3.1. Distance determination

Assigning a distance to sources detected with a photometer is a crucial step in the process of giving physical significance to all information extracted from Hi-GAL data. While reliable distance estimates are available for a limited number of known objects (as, e.g., HII regions, see Russeil 2003, and masers, see e.g. Green & McClure-Griffiths 2011) this information does not exist for the majority of Hi-GAL sources. We adopted the scheme presented by Russeil et al. (2011) aiming to assign kinematic distances to large lists of sources: a ^{12}CO (or ^{13}CO) spectrum (e.g., from the BU-FCRAO Galactic Ring Survey, or GRS, Jackson et al. 2006) is extracted at the line of sight of every Hi-GAL source and the VLSR of the brightest spectral component is assigned to it, allowing the calculation of a kinematic distance (see details below). Using extinction maps (derived from the 2MASS point source catalogue, see e.g. Schneider et al. 2011) and a catalogue of sources with known distances (HII regions, masers and others) the distance ambiguity is resolved and a recommendation is given. In this way it is possible to produce a

¹ The Arecibo Observatory is part of the National Astronomy and Ionosphere Center, which is under a cooperative agreement with the National Science Foundation.

² <http://www.exelisvis.com/ProductsServices/IDL.aspx>

³ CLASS is part of the GILDAS software package developed by IRAM.

Table 1: 6.7-GHz methanol masers detected with the Arecibo telescope. V_{\min} and V_{\max} represent the minimum and maximum velocity corresponding to the range of emission of the maser. S_{pk} represents the peak flux density, and $\int S_{\nu} dV$ is the integrated flux density in the velocity range $[V_{\min}, V_{\max}]$. d is the estimated distance of the Hi-GAL source. The 8th and 9th columns show the nearest Hi-GAL source (if the angular separation is ≤ 200 arcsec) for crowded fields, and the corresponding angular separation. In this case they are either the same source or there is likely some contamination from the sidelobes. The 11th column indicates whether the maser is a new detection (Y) or it is instead a known source (N). Source names in boldface indicate an OH maser counterpart determined using both positional and velocity association criteria (see Table 2).

Name	RA [J2000.0]	DEC [J2000.0]	V_{\min} [km s ⁻¹]	V_{\max} [km s ⁻¹]	S_{pk} [Jy]	$\int S_{\nu} dV$ [Jy km s ⁻¹]	Nearest source	Ang. separ. [arcsec]	d [kpc]	New?	Ref. ^a
G32.14+0.13	18:49:32.5	-00:38:09	92.3	93.2	0.03	0.01	G32.11+0.09	189	6.1	Y	–
G32.11+0.09	18:49:37.7	-00:41:01	90.2	104.5	1.16	0.77	G32.14+0.13	189	5.2 ^b	N	S1999
G32.74-0.07	18:51:21.8	-00:12:05	24.1	47.9	47.96	107.08	–	–	2.5	N	CAS1995
G33.09+0.06	18:51:30.5	00:10:41	77.9	84.9	0.14	0.09	–	–	5.3	Y	–
G32.82-0.08	18:51:32.1	-00:07:52	58.4	60.3	0.05	0.04	–	–	5.9	Y	–
G33.13-0.09	18:52:07.9	00:08:14	70.4	82.2	11.36	14.47	–	–	4.9	N	SHK2000
G33.41-0.00	18:52:20.1	00:25:48	97.0	108.2	0.43	0.83	–	–	–	N	SHK2000
G33.59-0.03	18:52:46.0	00:34:10	102.6	103.5	0.02	0.01	G33.61-0.03	107	–	Y	–
G33.61-0.03	18:52:49.0	00:35:47	102.8	103.8	0.07	0.05	G33.59-0.03	107	6.5 ^b	Y	–
G33.65-0.02	18:52:50.2	00:37:40	101.6	103.7	0.06	0.04	G33.61-0.03	114	4.5	Y	–
G34.37+0.23	18:53:13.6	01:23:31	54.9	63.7	1.63	0.99	–	–	1.6 ^b	N	SHK2000
G34.08+0.01	18:53:30.5	01:02:04	54.7	61.6	0.73	0.55	–	–	3.7	N	SKH2002
G35.46+0.13	18:55:34.2	02:19:11	73.2	74.4	0.02	0.01	–	–	5.1	Y	–
G34.19-0.59	18:55:51.2	00:51:19	57.6	63.1	0.22	0.18	–	–	3.8	Y	–
G35.57-0.03	18:56:22.6	02:20:28	127.0	127.6	0.02	0.01	–	–	10.4	Y	–
G34.71-0.59	18:56:48.2	01:18:46	77.8	80.0	0.01	0.00	–	–	–	Y	–
G35.13-0.74	18:58:06.0	01:37:07	26.1	40.8	31.90	34.52	G35.14-0.75	62	2.2 ^b	N	SHK2000
G35.14-0.75	18:58:09.9	01:37:27	26.2	39.4	1.70	1.80	G35.13-0.74	62	2.3	N	SHK2000
G36.42-0.16	18:58:23.2	03:02:11	71.4	72.3	0.03	0.01	–	–	8.6	Y	–
G36.83-0.02	18:58:39.0	03:28:01	52.7	64.5	2.51	6.35	–	–	3.9	N	PGD2007
G37.04-0.03	18:59:04.2	03:38:34	77.9	86.5	9.56	17.61	–	–	5.6	N? ^c	SKH2002, PGD2007
G37.34-0.06	18:59:43.1	03:53:40	51.3	52.6	0.02	0.01	–	–	9.8	Y	–
G37.19-0.41	19:00:43.4	03:36:24	29.4	30.1	0.07	0.02	–	–	11.1	Y	–
G37.86-0.60	19:02:36.0	04:07:04	49.3	54.2	0.19	0.25	–	–	3.4	Y	–
G38.93-0.36	19:03:42.0	05:10:24	31.0	33.8	0.04	0.05	–	–	2.7	N	SHK2000
G39.99-0.64	19:06:39.9	05:59:14	71.5	72.1	0.02	0.01	–	–	4.3	Y	–
G41.13-0.19	19:07:10.2	07:12:17	55.6	63.8	0.03	0.01	G41.16-0.18	106	4.3	Y	–
G41.16-0.18	19:07:11.2	07:14:02	55.6	63.6	0.07	0.08	G41.13-0.19	106	4.2	Y	–
G41.05-0.24	19:07:12.4	07:06:25	65.0	65.7	0.12	0.04	–	–	8.1	Y	–
G43.10+0.04	19:09:59.7	09:03:58	8.8	10.1	0.02	0.02	–	–	11.1 ^b	Y	–
G43.53+0.01	19:10:52.9	09:25:44	51.6	52.9	0.09	0.03	–	–	–	Y	–
G47.04+0.25	19:16:41.5	12:39:20	101.5	102.0	0.02	0.00	–	–	4.7	Y	–
G45.87-0.37	19:16:42.9	11:19:10	59.6	60.5	0.02	0.01	–	–	5.2	Y	–
G46.32-0.25	19:17:09.0	11:46:24	41.5	41.9	0.02	0.01	–	–	7.4	Y	–
G56.96-0.23	19:38:16.8	21:08:07	29.3	30.6	1.12	0.42	–	–	3.0	Y	–
G59.78+0.63	19:41:03.0	24:01:15	36.2	40.6	0.03	0.03	–	–	2.1	Y	–
G59.63-0.19	19:43:49.9	23:28:37	21.9	32.8	0.58	0.51	–	–	2.3	Y	–

Notes. ^(a) S1999, Slysh et al. (1999). CAS1995, Caswell et al. (1995). SHK2000, Szymczak et al. (2000). SKH2002, Szymczak et al. (2002). PGD2007, Pandian et al. (2007). ^(b) Distance determined from the BeSSeL Survey (see Section 3.1). ^(c) This source has an angular distance of about 80 arcsec from source G37.02-0.03 observed by SKH2002 and PGD2007, but the spectra are not similar. Emission partially overlaps only between 78 and 80 km s⁻¹. PGD2007 also detects some weak emission at about 85 km s⁻¹.

Table 2: Same as Table 1 for the 6.0-GHz OH masers detected with the Arecibo telescope. Source names in boldface indicate a methanol maser counterpart (see Table 1).

Name	RA [J2000.0]	DEC [J2000.0]	V_{\min} [km s ⁻¹]	V_{\max} [km s ⁻¹]	S_{pk} [Jy]	$\int S_{\nu} dV$ [Jy km s ⁻¹]	d [kpc]	New?
G32.74-0.07	18:51:21.8	-00:12:05	25.1	39.2	0.56	0.978	2.5	N
G33.70+0.28	18:51:50.4	00:49:06	24.3	26.0	0.03	0.029	2.6	Y
G33.13-0.09	18:52:07.9	00:08:14	72.2	79.9	0.04	0.037	4.9	N
G34.13+0.07	18:53:21.3	01:06:11	62.1	62.2	0.02	0.006	3.8	Y
G35.74+0.15	18:56:01.0	02:34:34	81.8	85.8	0.02	0.031	5.6	Y
G35.57-0.03	18:56:22.6	02:20:28	81.1	87.0	0.04	0.086	10.4	N
G34.71-0.59	18:56:48.2	01:18:46	81.8	85.0	0.02	0.031	–	Y
G35.13-0.74	18:58:06.0	01:37:07	32.8	37.1	3.92	3.615	2.2	Y
G37.81+0.41	18:58:53.9	04:32:15	18.1	18.4	0.04	0.009	1.2	Y
G35.29-0.89	18:58:57.0	01:41:40	57.6	58.5	0.04	0.019	2.5	Y
G37.04-0.03	18:59:04.2	03:38:34	81.1	85.1	0.05	0.073	5.6	Y
G59.63-0.19	19:43:49.9	23:28:37	66.7	67.2	0.01	0.004	2.3	Y

“distance map” having the same pixel size of the CO cube used to extract the spectra for every target, where the value of the pixel is the assigned distance of the Hi-GAL source(s) falling in that pixel.

A source of error comes from the use of extinction maps to solve for the distance ambiguity. A comparison between distances to methanol maser sources assigned using extinction maps and HI self-absorption, suggests that the former method tends to assign more often the far heliocentric distance (Pestalozzi et al., *in prep.*). The effects of this incorrect distance assignment are more severe the larger the difference between near and far heliocentric distances, because of the square dependence of mass and luminosity on the source distance. For the present paper however, we have to rely on the use of extinction maps for practical reasons and also because for most of the sources no spectral line emission has been observed other than what can be extracted from the GRS data cube (Jackson et al. 2006).

We also checked if there was some overlapping between our sample of Hi-GAL clumps and the sources observed in the BeSSeL Survey⁴ (“Bar and Spiral Structure Legacy Survey”, Brunthaler et al. 2011). We found only 4 methanol masers with a BeSSeL source within 5 arcmin (an additional source is within 12 arcmin), and in all these cases the distance determined by the BeSSeL team was *smaller* than that determined by us with the method described above, by a factor 0.19 to 0.85 (see Reid et al. 2009). Clearly, if this trend will be confirmed, it will make these masers even weaker (see Section 4.1).

3.2. New methanol and OH masers

Out of a sample of 107 observed Hi-GAL sources we detected a total of 32 methanol masers (30% detection rate), with 22 sources being *new* detections, in the Galactic longitude range [32°.0, 59°.8]. We also detected 12 6.035-GHz OH maser (11% detection rate), with 9 objects being new detections. Only one of the newly detected methanol masers (G34.71-0.59) has an associated OH maser. The J2000.0 positions, velocity range of maser emission [V_{\min} , V_{\max}], peak flux density, S_{pk} , integrated flux density, $\int S dV$, and the estimated distance, d , for each source are given in tables 1 and 2, for the methanol and OH masers, respectively. Table C.1 lists instead the Hi-GAL sources where no methanol maser was detected, and we report for each source the RMS of the final spectrum.

The positions of the new detected methanol and OH masers are graphically shown in the top panel of Fig. 1, where a higher concentration of sources is clearly seen around $l \approx 35^\circ$ and $b \approx 0^\circ$, where giant molecular clouds can be found that contain the W44 supernova remnant (e.g., Reach et al. 2005). We note that a total of 7 maser sources are found outside the galactic latitude range $|b| \leq 0.5$, which was explored by the AMGPS survey. We also note that Green et al. (2010) found that 97% of their MMBS sources were at a latitude within 1° of the Galactic plane.

As a comparison, Fig. 1 also shows the positions of the UC H II regions, a typical signpost of HMSF, from the CORNISH catalog (Hoare et al. 2012, Purcell et al. 2013). One can note that the methanol masers follow the general distribution of the UC H II regions, and in some cases their positions are clearly coincident. In fact, we find that 7 methanol masers have a UC H II region within 45 arcsec (i.e., about one Arecibo beam). Three of these masers (G32.74-0.07, G33.13-0.09 and G33.41-0.00) were already known (see Table 1), whereas the other four are new and lower flux density masers (G34.19-0.59, G35.46+0.13, G35.57-0.03 and G37.86-0.60). Although the nature of this association will have to be further investigated through higher-angular resolution observations, we see that most of our newly detected methanol masers do *not* have an associated UC H II region (at the sensitivity level of the CORNISH catalog). This result suggests that masers like these are more likely associated with the *pre*-UC H II phase of HMSF.

The bottom panel of Fig. 1 shows longitudes and velocities of all maser sources detected at Arecibo. Since 6.7-GHz methanol masers are only detected towards regions of HMSF (e.g., Pestalozzi et al. 2002) they are expected to be found within spiral arms. We find that the median (mean) velocity of all masers (methanol and OH) is $60.0 \pm 20.7 \text{ km s}^{-1}$ ($61.9 \pm 20.8 \text{ km s}^{-1}$). Five sources have velocities smaller than 30 km s^{-1} , while there is only one source with a velocity exceeding 120 km s^{-1} . By comparison with the velocity-longitude plot of Pandian et al. (2007) we can see that we have a main group of sources, with $l \sim 35^\circ$ to 40° and $V_{\text{lsr}} \sim 60 \text{ km s}^{-1}$ to 80 km s^{-1} , which fall near the Carina-Sagittarius arm. Another, less numerous group of sources, can be found near the overlapping region between the Carina-Sagittarius and Perseus arms. We also note that a significant fraction of the masers do not lie near any spiral arm loci, a phenomenon already discussed by Pandian & Goldsmith (2007) and Green et al. (2010). This fact may be related with the results of Reid et al. (2009), who found that on average the HMSF regions orbit the Galaxy $\approx 15 \text{ km s}^{-1}$ slower than the Galaxy spins.

⁴ <http://www3.mpifr-bonn.mpg.de/staff/abrunthaler/BeSSeL/>

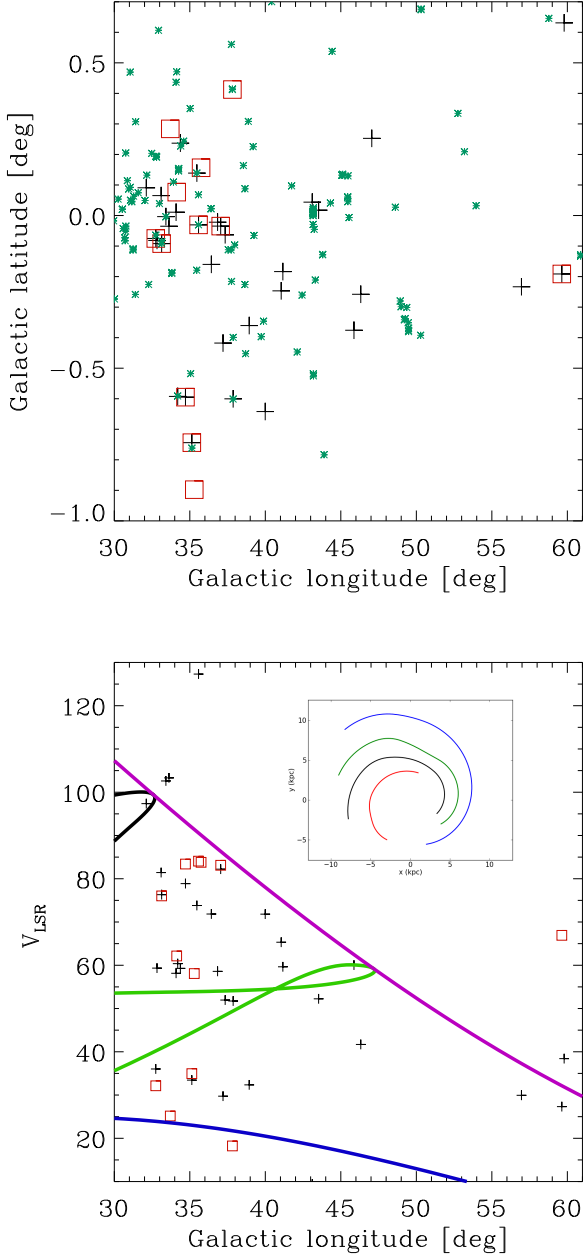


Fig. 1: *Top panel.* Region searched for maser counterparts to Hi-GAL sources. Methanol maser detections are denoted by “+” signs and OH maser detections are denoted by red squares. Also shown are the UC H II regions from the CORNISH catalog (green asterisks). The concentration of sources around $\ell \approx 35^\circ$ and $b \approx 0^\circ$ is near the W44 region. *Bottom panel.* Longitude-velocity distribution of all masers detected at Arecibo. The coloured loci represent the spiral arms and correspond to those shown in the inset: Norma (red), Scutum (black), Sagittarius (green), Perseus (blue). The locus of the tangent point is shown in purple.

Fig. A.1 shows that the spectra of the masers are composed of many spectral features spread over a range of velocities. The total velocity spread in an individual source depends on the sensitivity of the observation, particularly when attempting to observe weak masers, and may also change as a result of intrinsic

variability of the components. The median (mean) spread in velocity for the methanol and OH masers, respectively, is 2.8 km s^{-1} (5.4 km s^{-1}) and 3.1 km s^{-1} (5.0 km s^{-1}). A large velocity range ($\geq 15 - 20 \text{ km s}^{-1}$) may also be caused by different maser sources falling within the Arecibo beam. For example, the methanol maser source G32.82-0.08 has a component near 60 km s^{-1} and another near 30 km s^{-1} , yielding a velocity range of about 23 km s^{-1} . However, the only new maser component is the one at higher velocity, whereas the component at $\approx 30 \text{ km s}^{-1}$ is likely to be contamination from the known methanol maser G32.74-0.07, which has itself a large velocity range. Another example of contamination in the beam is described in the next section.

3.3. Cross-scans and Long-integration observations

During our observations at Arecibo we selected several sources (see Table 3) to perform a cross-scan centered around the nominal Hi-GAL position and with 24 arcsec (about half beam) angular steps. Table 3 shows the results obtained at various dates, and in the case of source G41.16-0.18 it also shows that different offsets were obtained depending on the *velocity component* used for the computation (see Fig. 2). This is clearly an indication that distinct spatial maser components were simultaneously present within the Arecibo beam, which can only be evidenced during a cross-scan. The results listed in Table 3 show that in most cases the maser was observed within the main beam, and the estimated offset was less than or comparable with the Arecibo telescope pointing errors ($\lesssim 15$ arcsec, see Section 2.3), except on June 5th, 2013, when the estimated offset was quite large.

An interesting question is that of multiple velocity maser components in the low- and high-flux density masers (see Section 4.3). Therefore, in a few selected low-flux density masers (G45.87-0.37, G43.53+0.01, G59.78+0.63) we performed several consecutive 5 min scans (totalling 15 – 25 min integration time), that we then averaged in order to check for multiple maser components that could have escaped the single 5 min integrations because of sensitivity limitations. The selected sources all initially appeared to have a single component spectrum (G45.87-0.37, G43.53+0.01) or had just a few components occupying a small ($\lesssim 5 \text{ km s}^{-1}$) range of velocities (G59.78+0.63). Our long-integration spectra of these sources did *not* show any new component.

In addition to sensitivity, another possible explanation for the non-detection of multiple velocity components is that the source is being observed off-peak, leaving only the most intense component detectable. In this regard we note that sources G45.87-0.37 and G59.78+0.63 were also observed in cross-scan mode, as described in the previous section and in Table 3. Therefore, the long-integration scans were performed toward the observed peak position of the 5-pointings cross-scans. The observed peak positions turned out to be very close to the estimated actual positions of the sources. Despite this adjustment, we still did not observe any additional velocity component. This test toward a very small number of sources is neither complete nor conclusive, and more sensitive observations toward a larger sample of low-flux density methanol masers are clearly needed to resolve this issue. However, we can use this result as a tentative indication that the weak methanol masers detected at Arecibo do indeed tend to have fewer velocity components than previously observed brighter masers (see also Section 4.3).

Table 3: Results of cross-scans performed at Arecibo.

Source	Date observed	Velocity component [km s ⁻¹]	Δ RA [arcsec]	Δ DEC [arcsec]	Total offset [arcsec]
G37.86-0.60	26-Jan-2013	51.1	-0.7	2.0	2.2
G56.96-0.23	21-Jan-2013	29.8	8.2	8.8	12.0
G41.16-0.18	30-May-2013	56.0	6.8	4.1	7.9
G41.16-0.18	30-May-2013	62.8	0.7	-2.7	2.8
G41.05-0.24	30-May-2013	65.4	8.5	-11.1	13.9
G59.63-0.19	31-May-2013	29.6	0.8	-6.0	6.0
G59.78+0.63	31-May-2013	38.3	11.9	14.5	18.7
G45.87-0.37	05-Jun-2013	59.9	22.1	17.0	29.9

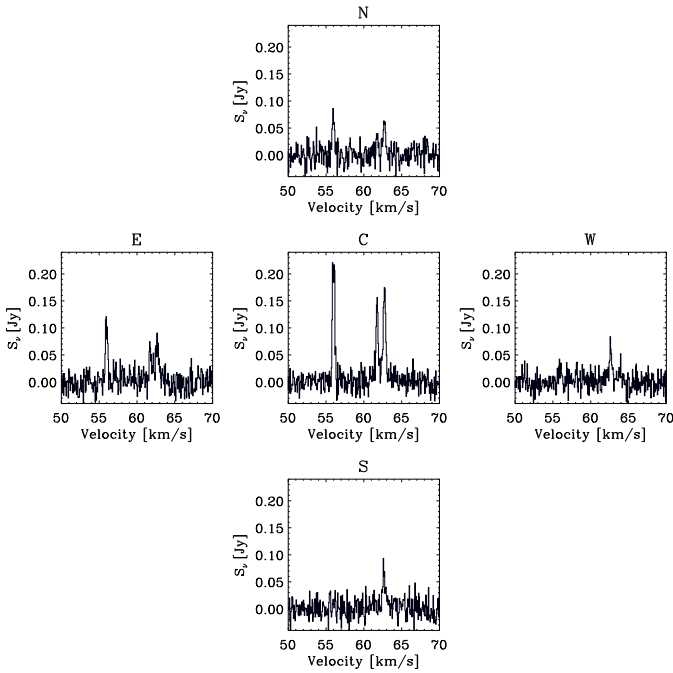


Fig. 2: Cross-scan (with 24 arcsec angular step) performed on source G41.16-0.18, showing different velocity components and their variation as a function of position.

3.4. Variability

In order to test the variability of the methanol masers detected by us, we have observed some of the sources at different dates, and we have selected both weak and relatively bright masers. In Fig. 3 we show the methanol spectra observed in at least two different dates (e.g., July 2012 or January 2013, and May or June 2013). The sources showing the greatest variation in intensity are G41.16-0.16, G59.63-0.19, G59.78+0.63 and, to a lesser degree, G41.05-0.24. The other sources show variations $\lesssim 20\%$ (see Table 4) which could be accounted for by calibration and pointing uncertainties.

In sources G33.13-0.09 and G41.16-0.16 we note the greatest difference between the variation of the peak flux density and the total flux integrated over all velocity components. Thus, not all of the observed maser components have varied by the same amount during the period considered, either because they effectively vary differently with time, or because they do not belong to the same source. In the specific case of G41.16-0.16, given the

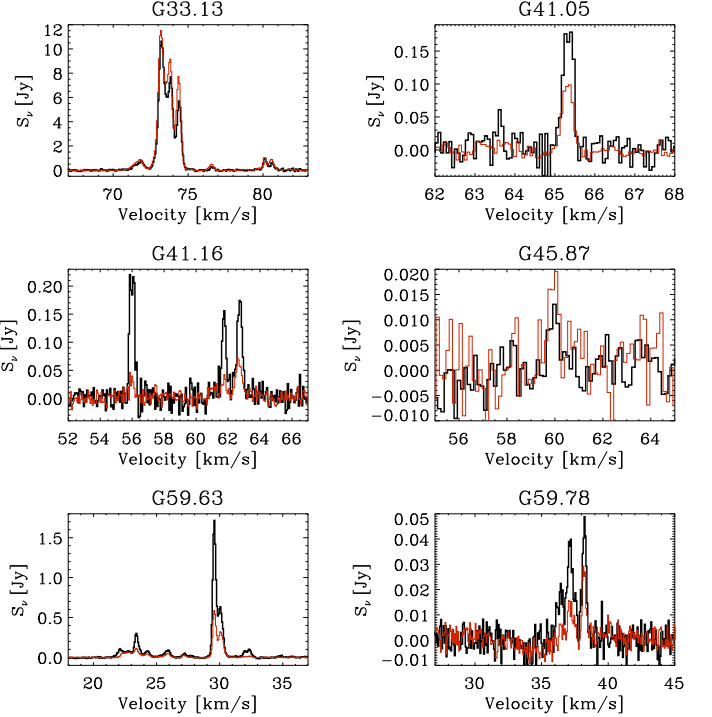


Fig. 3: Spectra of methanol masers observed at different dates, with red (thin) and black (thick) solid line representing older and more recent spectra, respectively.

results of the cross-scan performed on this source (Section 3.3), we favour the second alternative.

4. Discussion

4.1. Intrinsic maser intensity

As we already mentioned in Section 2.1, Pandian & Goldsmith (2007) found that the maximum of the distribution of their methanol masers as a function of flux density occurred for peak flux densities between 0.9 and 3 Jy. Fig. 4 shows that the peak flux density distribution of the 6.7-GHz methanol masers detected toward our sample of Hi-GAL sources does not follow the distribution found by Pandian & Goldsmith (2007). This is not surprising since our sensitivity is better than previous surveys, and we have excluded from our analysis already known strong methanol masers.

But, clearly the interesting question is whether also the *intrinsic* intensity of these masers is lower than that of previously known methanol masers. In fact, the simplest explanation of

Table 4: Variability of a few selected methanol masers. Columns n.5 and 6 list the percentage difference of the peak flux density (at the velocity indicated in column n.4) and of the total flux between the initial and final dates of observation.

Source	Initial Date observed	Final date observed	Velocity component [km s ⁻¹]	Flux density variation [%]	Flux variation [%]
G33.13-0.09	July 2012	May 2013	73.3	-7.6	-16.6
G41.05-0.24	July 2012	May 2013	65.4	41.6	34.9
G41.16-0.18	January 2013	May 2013	56.0	379.5	134.6
G43.10+0.04	January 2013	May 2013	9.5	9.1	8.3
G45.87-0.37	January 2013	May 2013	60.0	-31.6	-33.3
G59.63-0.19	July 2012	May 2013	29.6	202.0	158.8
G59.78+0.63	July 2012	May 2013	38.3	96.3	107.4

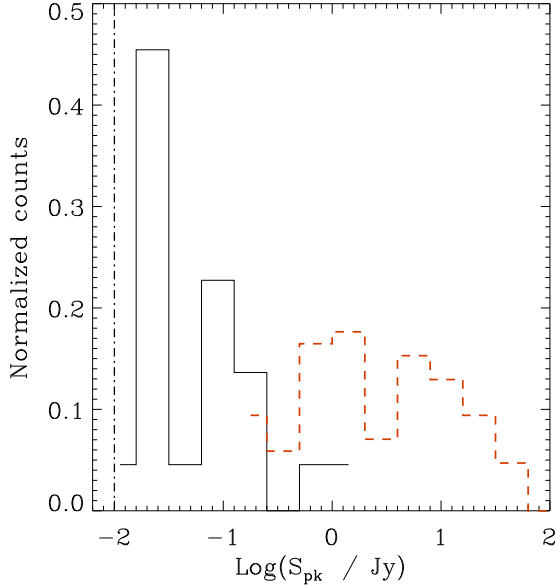


Fig. 4: Histogram of the normalized counts (number of sources per bin divided by the total number of sources) vs. peak flux for the new methanol masers detected at Arecibo (black solid line) and for the AMGPS (Pandian et al. 2007, 2009; red dashed line). The rms noise level in our spectra was $\sim 5 - 10$ mJy (shown by the dash-dotted vertical line) in each spectral channel (see Table C.1).

the weakness of our masers would be that, for example, most sources in our Hi-GAL sample are systematically more distant than the sources observed by Pandian et al. (2007). However, we can exclude this observational selection effect because Fig. 5 clearly shows that although both source samples approximately cover the same distance range, the AMGPS masers are clearly shifted towards higher integrated flux densities, with a median value which is about 50 times higher than that of our sample. In addition, we have seen in Section 3.1 that where a BeSSeL counterpart exists, its distance is smaller than that determined by us.

Another possibility to explain the difference shown in Fig. 5, would be to assume that the low brightness of our sources is caused by the masers being systematically offset with respect to the nominal position of the Hi-GAL source, or even by observing a known methanol maser in a sidelobe of the Arecibo beam. It seems very unlikely that *all* of the weak masers detected by us have been observed with such a large pointing offset to fully

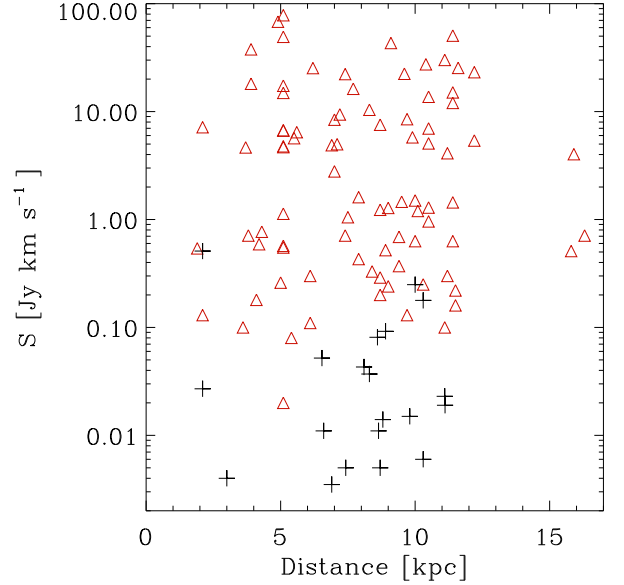


Fig. 5: Plot of the methanol maser flux vs. distance of the associated clump for all masers found by Pandian et al. (2007) (red triangles) and our *newly detected* methanol masers (black “+” signs). The median value of the integrated flux density of our own masers is ≈ 0.03 Jy km s⁻¹, while the median value for the AMGPS masers is ≈ 1.6 Jy km s⁻¹.

justify their lower intensity. In fact, the cross-scans discussed in Section 3.3 and listed in Table 3, show that the typical measured offset may account for at most a $\approx 25\%$ decrease of the maser peak intensity and thus cannot justify the difference of about a factor of 50 between the median values of the integrated flux densities previously mentioned.

Figure 6 indeed suggests that our methanol masers are intrinsically weaker than those detected in the AMGPS. In the top panel, the normalized histogram of the peak flux density multiplied by the distance squared, $S_{\text{pk}} \times d^2$, shows a pronounced peak at small values for our methanol masers. Given that the AMGPS and our samples have similar number of sources, we do not expect statistical fluctuations to affect this comparison. We also note that the lowest bins of the AMGPS may be affected by completeness (Pandian et al. 2009), whereas our distribution is robust even in the lowest bins, since it is a pointed survey.

Figure 7 represents a similar plot to that shown in Fig. 6, but for the excited OH masers. In this case the comparison is done with the survey of Caswell & Vaile (1995). In Fig. 6 the

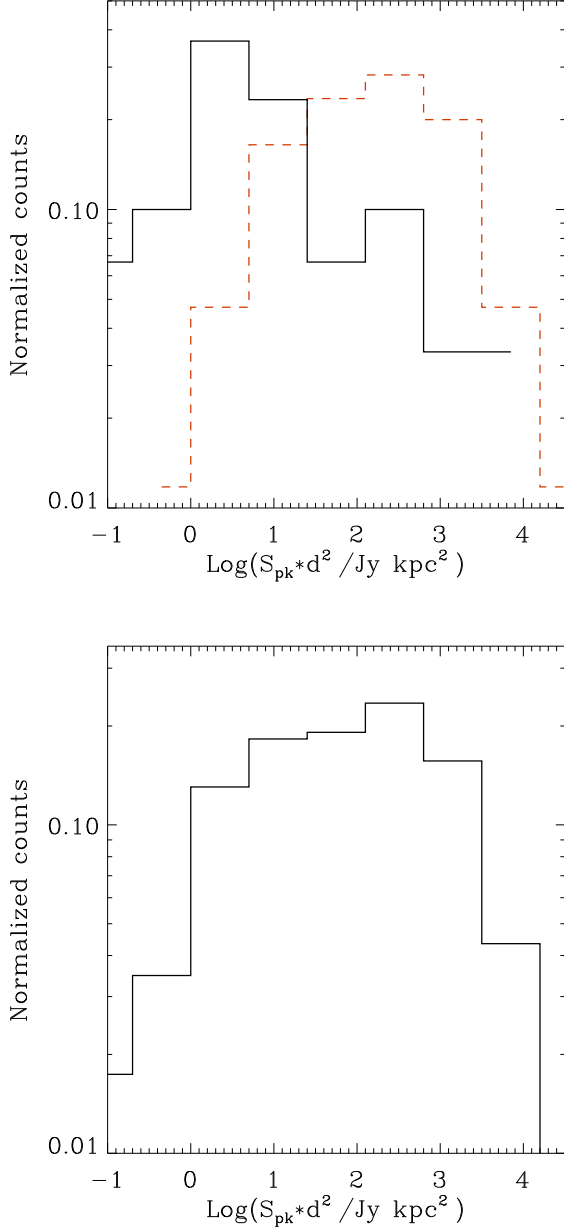


Fig. 6: *Top panel.* Histogram of the normalized counts (number of sources per bin divided by the total number of sources) vs. $S_{\text{pk}} \times d^2$, for both the Pandian et al. (2007, 2009) data (red dashed line) and our own results (black solid line), including new and known methanol masers. *Bottom panel.* Histogram of the normalized counts vs. $S_{\text{pk}} \times d^2$ of all methanol masers from both our survey and the AMGPS.

distribution of the methanol masers detected by us has clearly its peak shifted toward smaller values of $S_{\text{pk}} \times d^2$, compared to the reference distribution. Figure 7 also seems to suggest a similar shift to lower intensities for our OH masers, but given the much lower number of detections this cannot yet be considered a firm conclusion. Both figures 6 and 7, however, indicate that our blind survey toward Hi-GAL sources was indeed more sensitive to the low-intensity tail of the distribution of methanol and OH maser intensities.

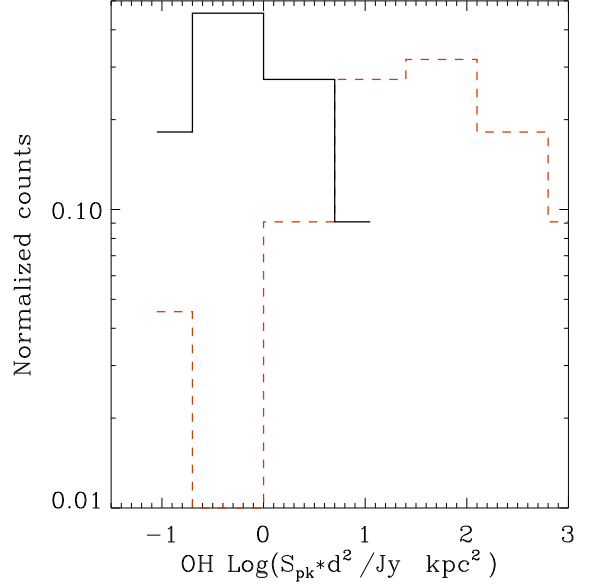


Fig. 7: Histogram of the normalized counts (number of sources per bin divided by the total number of sources) vs. $S_{\text{pk}} \times d^2$ of the OH masers, for both the Caswell & Vaile (1995) data (red dashed line) and our own results (black solid line). The bin width has been increased compared to Fig. 6.

4.2. Masers luminosity function

Using the kinematic distance one can also calculate the isotropic luminosities of the masers (using their integrated flux densities, S) and the methanol maser luminosity function. The top panel of Fig. 8 shows the luminosity function of 6.7-GHz methanol masers, compared with the luminosity function of the AMGPS masers (Pandian et al. 2009). An interesting feature of Fig. 8 is that the peak of our distribution nicely overlaps with the bins of the AMGPS distribution which may be affected by completeness effects. Therefore, in the bottom panel of Fig. 8 we plot the distribution obtained by merging our sample with the AMGPS masers. We note that since the counts at luminosities $L < 10^{-7} L_{\odot}$ come mainly from our data, they are not affected by completeness effects and thus the turnover at low luminosities (but still higher than the minimum measured luminosity) is real. The shape of the merged distribution of the $S_{\text{pk}} \times d^2$ parameter, shown in the bottom panel of Fig. 6, is somewhat different from the luminosity function, featuring an approximately flat-top with decreasing tails.

While the luminosity functions and the distributions of the $S_{\text{pk}} \times d^2$ parameter bear some resemblance, they are not expected to be exactly the same, since the latter does not take the linewidths and multiple emission components into account. The luminosity of the maser emission is supposed to be a more reliable indicator of the physical conditions in a region as it depends on the conditions over a larger gas volume and will be less influenced by the fluctuations responsible for the intensity of a single spectral peak. On the other hand, one might also think that the intrinsic sensitivity of the quantity $S_{\text{pk}} \times d^2$ to the main (or single) component of the maser emission would make this parameter better suited for a comparison of the relative strength between our maser sample and the AMGPS masers.

For example, this might be the case if the luminosity of the weak masers ($S_{\text{pk}} \ll 1$ Jy) were systematically underestimated

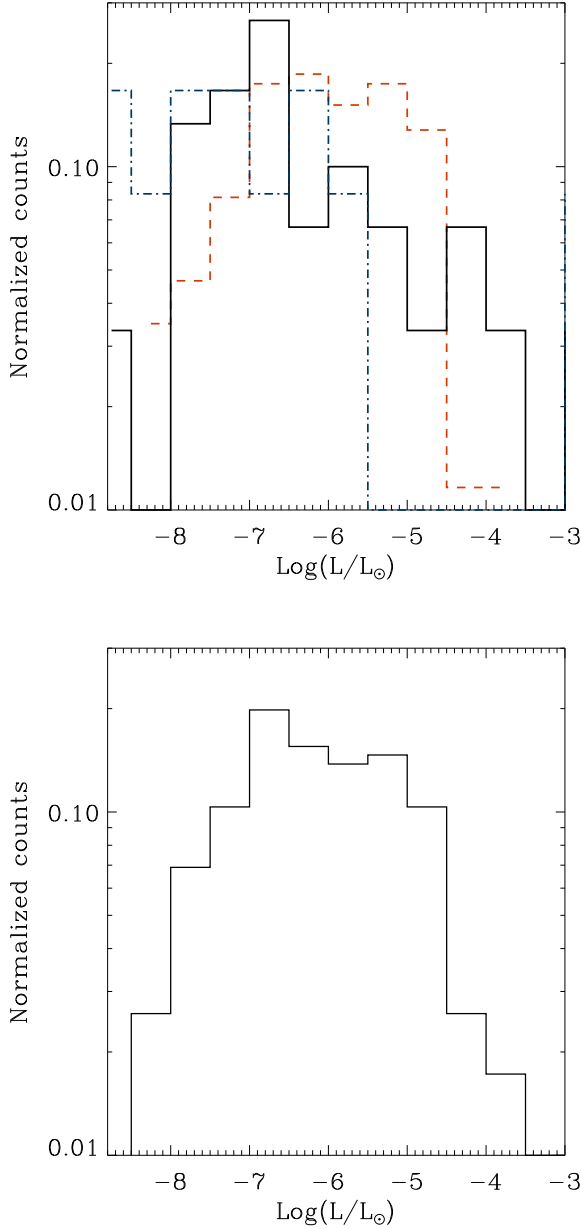


Fig. 8: *Top panel.* Histogram of the normalized counts (number of sources per bin divided by the total number of sources) vs. luminosity of the methanol masers, for both the Pandian et al. (2007, 2009) data (red dashed line) and our own results (including new and known masers) with the luminosity of both the methanol (black solid line) and OH masers (blue dash-dotted line). *Bottom panel.* Histogram of the normalized counts vs. luminosity of *all* methanol masers from both our survey and the AMGPS.

because the sensitivity of the observations is not good enough to detect all multiple emission components. The top panel of Fig. 9 would appear to support this assumption, since the masers with the lowest S_{pk} are also characterized by a lower velocity range, or actually show only one emission component. However, the middle panel of Fig. 9 shows that also the integrated flux density follows the same behaviour. In both cases we have used the Bayesian IDL routine LINMIX_ERR to perform a linear regres-

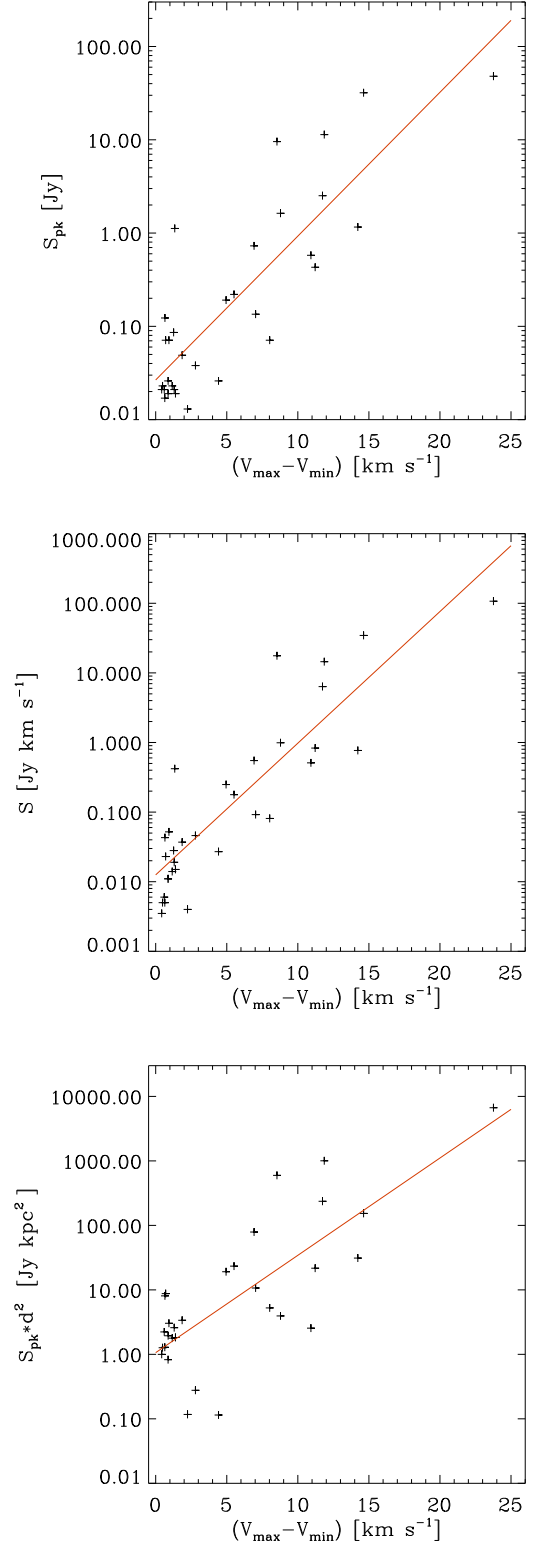


Fig. 9: *Top panel.* Plot of the peak flux density of the methanol masers vs. the difference between the maximum and minimum value of the velocity range of emission. The solid line represents the linear fit (from Bayesian statistics, see text) to all points. The Spearman rank coefficient is 0.75. *Middle panel.* Same as above but with the integrated flux density, S , plotted vs. the velocity range. The Spearman rank coefficient is 0.88. *Bottom panel.* Same as above but with the $S_{\text{pk}} \times d^2$ parameter plotted vs. the velocity range. The Spearman rank coefficient is 0.69.

sion, to find the slope of the best fit line. The relatively high correlation for the plots in the top and middle panels of Fig. 9 suggests that the integrated flux density is mostly determined by the most intense emission component.

Therefore, the luminosity function, or the distribution of the $S_{\text{pk}} \times d^2$ parameter, of the methanol masers found toward our sample of Hi-GAL dust clumps, shows a markedly different shape compared to that, for example, of the AMGPS masers. The luminosity function is also different from that estimated by Pestalozzi et al. (2007) for the whole Galaxy. Although our sample is admittedly still small, this result is suggesting that the luminosity of the methanol masers detected towards our sample of Hi-GAL sources is not distributed according to the luminosity function observed in unbiased surveys. Fig. 8 also shows the luminosity function of the 6.0-GHz OH masers, which is more uncertain due to the low number of OH masers detected. The range of OH luminosities is similar to that of the methanol masers, but no other trend is visible, and a more detailed comparison with the luminosity function of the methanol masers cannot be done with these data alone.

4.3. Properties of associated Hi-GAL clumps

Previous works have already attempted to find possible correlations between the physical parameters of the gas/dust clump where maser activity is present and, e.g., the luminosity of the maser emission. Breen et al. (2010), for example, found that the 1.2-mm dust clumps with associated methanol masers have higher values of mass and radius than those with no associated 6.7-GHz methanol maser.

In Fig. 10 we present a luminosity vs. mass plot of all the Hi-GAL sources observed by us at Arecibo for which luminosity and mass could be calculated. These two physical parameters were determined using the estimated distance to the sources (see Section 3.1) and using a simple, single-temperature spectral energy distribution (SED) model to fit the PACS and SPIRE flux densities. Therefore, both luminosity and mass refer to the cold ($T_{\text{d}} \lesssim 20 - 30$ K) dust envelope of the Hi-GAL clumps (and should therefore be indicated as M_{env} and L_{env}), and may be insensitive to warmer dust (emitting mostly shortward of $\sim 24 \mu\text{m}$) if a central protostar (or cluster of protostars) has already formed within the clump.

In Fig. 10 one should thus be aware that the envelope luminosities may be *underestimating* the total (i.e., bolometric) clump luminosity, L_{bol} , if both warm and cold dust components exist within the Hi-GAL clump. With this *caveat*, in this figure we then show in different colors the groups of sources associated with a methanol or OH (or both) maser. It can be noted that while sources with only a methanol maser associated do not show any recognizable distribution pattern, sources with either just an OH maser or with both masers seem to occupy different regions in this plot. Hi-GAL clumps where *both* masers have been detected do show somewhat higher masses and luminosities. However, given our low number of sources and the fact that the internal structure of the Hi-GAL clumps is not yet known, these trends are not statistically significant.

Likewise, for these weak masers we are unable to find any evidence of the trends discussed by Breen et al. (2010). We note that their analysis is based on the data by Hill et al. (2005), whose angular resolution is comparable to that of the Hi-GAL maps. We have also estimated the gas density in the observed Hi-GAL clumps, with and without an associated methanol maser. The results are plotted in Fig. 11, which shows that no significant difference is observed between the distributions of sources

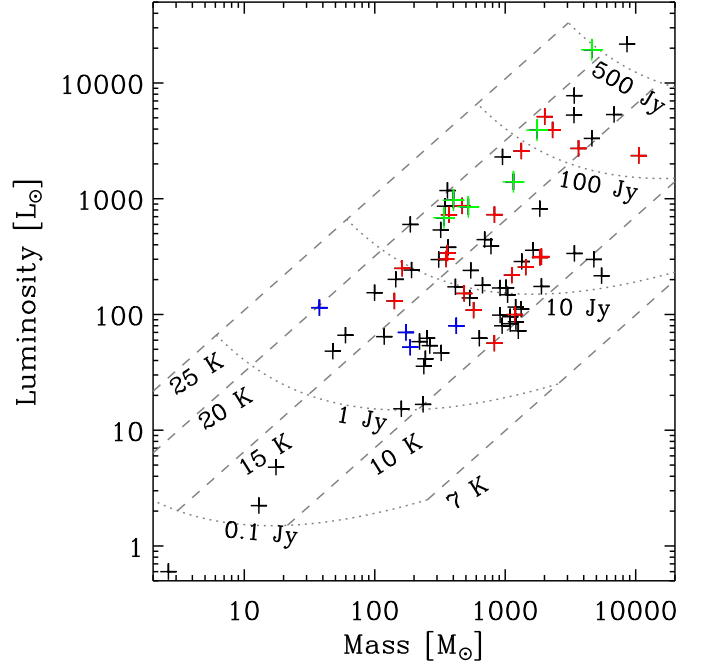


Fig. 10: Luminosity versus mass for all clumps (black “+” signs) observed at Arecibo, estimated using the distances listed in Table 1. Sources where a methanol or OH maser has been detected are shown in red and blue, respectively; sources with both masers are shown in green (both newly detected and previously known masers are shown). The dashed lines are loci at constant $T = 10, 20, 30,$ and 40 K. Roughly orthogonal to these are loci (dotted lines) of constant $250 \mu\text{m}$ flux density, ranging from 0.1 to 500 Jy (assuming a modified blackbody spectral energy distribution with $\beta = 1.5$ and a fixed, “typical” distance of ~ 6 kpc).

with and without a maser. These results are not too surprising, since dust clumps at distances ≥ 1 kpc, observed at relatively low angular resolution, may be still large enough to host more than one compact source, possibly in different evolutionary phases. Therefore, an improved analysis of the correlation between maser activity and the physical properties of the gas clump will be possible only through higher angular resolution maps of the molecular gas in the masers environment.

4.4. OH association

As we mentioned in Section 3.2 only one of the new methanol masers discovered by us has an associated excited OH maser, when the velocity range of the maser emission is also used as a criterion for the masers to be physically associated. However, if we also include the known methanol masers, then the number of sources with both maser types is 5 out of a total of 32 methanol masers. The main observational property that characterizes the sources where both types of maser activity is present, is the higher intensity of the methanol masers as compared to sources with no OH detection. In fact, Table 5 is tentatively suggesting (because of the large scatter) that both peak flux density and flux of methanol maser emission may have on-average higher values in sources associated with an OH maser. Although our sample is relatively small, and the scatter around the average values too high, this result is consistent with the findings

Table 5: Median values of peak and integrated flux density for *all* detected methanol masers.

All detections		Sources with OH maser		Sources without OH maser	
Median S_{pk}	Median $\int S \text{ d}V$	Median S_{pk}	Median $\int S \text{ d}V$	Median S_{pk}	Median $\int S \text{ d}V$
[Jy]	[Jy km s ⁻¹]	[Jy]	[Jy km s ⁻¹]	[Jy]	[Jy km s ⁻¹]
0.09	0.05	11.4	17.6	0.07	0.04

of Breen et al. (2010) toward a larger sample of more intense methanol and OH masers. We should note that the situation is not similar when one considers the OH masers (see Table 6). In fact, the median values of the peak flux density of the OH masers is comparable in sources with and without an associated methanol maser. Despite the *caveats* mentioned above, we can discuss our results in the context of maser excitation and compare them with proposed scenarios of maser evolution.

The model calculations of Cragg et al. (2002) showed that the coincidence of OH and methanol masers in many sources can be explained in terms of common excitation conditions which produce population inversions simultaneously in both molecules. The masers require infrared pumping radiation from warm ($T_d > 100$ K) dust and are most likely to form in cooler ($T_k < 100$ K) gas of moderately high density ($10^5 < n_H < 10^{8.3}$ cm⁻³). When methanol and OH masers are detected, it is necessary that both be present at high abundance in the gas phase. When masers of one or other molecule are seen in isolation, Cragg et al. (2002) gives two possible explanations; either the non-masing molecule is not sufficiently abundant, or the local conditions produce maser action in the favoured molecule alone.

These authors show that the 6.7-GHz methanol maser is excited at relatively lower densities ($n_H > 10^4$ cm⁻³), compared to the 6.035-GHz OH line (which requires $n_H \gtrsim 10^5 - 10^6$ cm⁻³), and is independent of gas density up to $n_H \sim 10^8$ cm⁻³. This indicates that the methanol maser excitation mechanism is predominantly radiative. On the other hand, the excitation of OH is more sensitive to the local density and also extends to higher densities, where the methanol maser is instead subject to collisional quenching. Cragg et al. (2005), however, showed that collisional quenching at high density of the 6.7-GHz methanol maser becomes less probable when new rate coefficients are used. Furthermore, it should be noted that the model calculations of Cragg et al. (2002) all refer to emerging masers with a brightness temperature exceeding 10⁴ K, or 0.1 Jy for a 6-GHz maser of size 0.7 arcsec. Therefore, their conclusions may not be entirely valid for weaker maser emission.

According to Cragg et al. (2002, 2005), there is therefore a limited range of conditions which favour maser action in just one molecule, and they claim that molecular abundance is likely the determinant factor of methanol and OH maser activity in HMSF regions. If that is indeed the case, then the presence or absence of both maser types should be able to be tied with the chemical evolution and age of the HMSF region. A common proposed scenario (Cragg et al. 2002, Ellingsen et al. 2011 and references therein) is that the gas-phase methanol abundance is enriched in maser regions following the evaporation of icy grain mantles. The same process is responsible for injecting water molecules in the gas-phase, then leading to production of OH through photodissociation or ion-molecule chemistry. This is consistent with a time-span when both masers are present, but chemical models (e.g., Charnley et al. 1992, 1995) predict that the OH abundance should peak after the methanol abundance has started to diminish (about 10⁵ yr after grain mantle molecules have been injected in the gas-phase). Therefore, methanol masers are expected to start

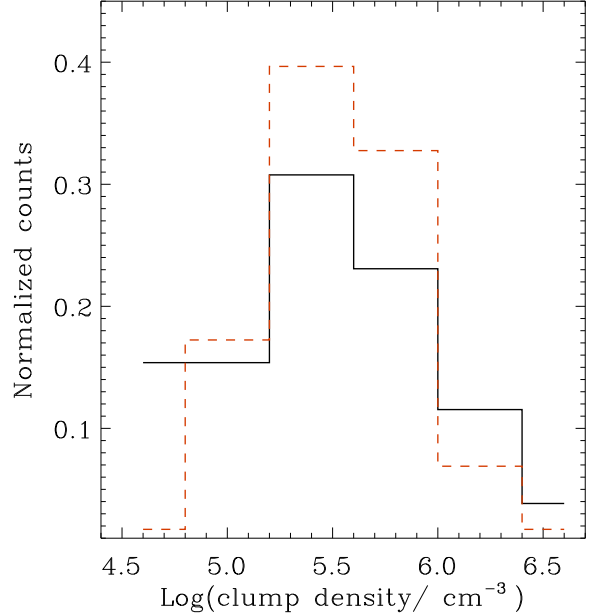


Fig. 11: Histogram of the density of *all* observed Hi-GAL clumps in our survey. The black (solid) and red (dashed) lines represent the distribution of sources with and without, respectively, an associated methanol maser.

(and finish) earlier than OH masers. We finally note that 2 of the 5 sources with double maser emission also show a MIPS 24 μ m counterpart.

4.5. IR counterparts

The association between mid-infrared emission and 6.7-GHz methanol masers has already been investigated in several of previous surveys. Recent works (e.g., Ellingsen 2006, Cyganowski et al. 2009, Pandian et al. 2011) have found a very close correspondence between 6.7-GHz methanol masers and mid-infrared emission, although it should be noted that in some cases (Ellingsen 2006, Cyganowski et al. 2009) these were targeted searches toward GLIMPSE point sources that resulted in high detection rates of 6.7-GHz methanol masers. However, even Pandian et al. (2011) found that almost all AMGPS 6.7-GHz methanol masers had indeed associated a MIPS 24 μ m counterpart within 5 arcsec.

We have thus searched for MIPS 24 μ m counterparts associated with our Hi-GAL sources, and found that 18 out of 32 methanol masers have a mid-infrared source within 5 arcsec (the median angular separation is 2.5 arcsec). Of the 22 new methanol masers 13 also have an associated MIPS 24 μ m counterpart, hence in our sample the fraction of sources with (IR-loud) or without (IR-quiet) a MIPS 24 μ m counterpart is about the same. We find no statistically significant difference between, for ex-

Table 6: Median values of peak and integrated flux density for *all* detected OH masers.

All detections		Sources with CH ₃ OH maser		Sources without CH ₃ OH maser	
Median S_{pk} [Jy]	Median $\int S \, dV$ [Jy km s ⁻¹]	Median S_{pk} [Jy]	Median $\int S \, dV$ [Jy km s ⁻¹]	Median S_{pk} [Jy]	Median $\int S \, dV$ [Jy km s ⁻¹]
0.04	0.03	0.05	0.07	0.03	0.02

ample, the median values of the $S_{\text{pk}} \times d^2$ parameter associated with either the IR-loud or IR-quiet sub-groups. However, Fig. 12 shows that, despite the large scatter, there seem to be a moderate correlation between the peak flux density of the methanol masers and the flux density of the associated MIPS 24 μm counterpart, which will need to be confirmed by future (high-angular resolution) observations. We note that the fraction of sources *without* mid-infrared emission is comparatively higher compared to the AMGPs masers. This fact, and the intrinsically weaker emission of our masers, must be carefully considered in the context of theoretical models for the maser excitation.

Clearly, the lack of association with mid-infrared emission may also be caused by sensitivity threshold and/or by optical depth effects. However, since Pandian et al. (2011) also searched for MIPS 24 μm counterparts, they were affected by the same effects and thus the differences between these two surveys become significant. It should also be noted that at present the analysis of the association between mid-infrared emission and our 6.7-GHz methanol masers may also be affected by the relatively large beam of the Arecibo telescope. In fact, the association rate that we have estimated is based on the *nominal* position of the Hi-GAL source which, as we have seen in Section 4.1, may not be precisely coincident with the maser position. In addition, each Hi-GAL clump may be generally composed by smaller cores, with different properties, and the core responsible for the maser emission may not necessarily be coincident with the core associated with the MIPS 24 μm counterpart. Therefore, a more detailed analysis of the mid-infrared association will require to actually map the masers (and, ideally, the Hi-GAL clumps as well) at higher angular resolution in order to determine their relative positions within the Hi-GAL clump and also with respect to the MIPS 24 μm counterpart. However, given all these *caveats* it is still quite surprising that we find the interesting (tentative) trend shown in Fig. 12.

4.6. Correlation between maser intensity and velocity range

Our previous discussion indicates that our blind survey of Hi-GAL sources is more sensitive to the low-flux density methanol masers that have escaped previous surveys. We have also seen in Section 4.4 that theoretical models suggest that the presence of a given maser type may be linked with the chemical evolution and age of the HMSF region, although this is difficult to verify observationally without higher angular resolution observations. However, even our observations have shown a peculiar and interesting correlation. In fact, Fig. 9 shows that the brightest masers tend to occur in regions with large velocity ranges, and viceversa. As discussed in Section 3.3, we can tentatively assume that the lack of multiple velocity components toward the less bright masers is not an observational effect due to limited sensitivity or positional offsets. Since maser emission is not isotropic but it is instead supposed to be highly beamed (Alcock & Ross 1985, Elitzur 1992), then in those regions with relatively few maser spots (and thus with a lower velocity range), we are less likely to observe any maser emission. In regions with many maser spots,

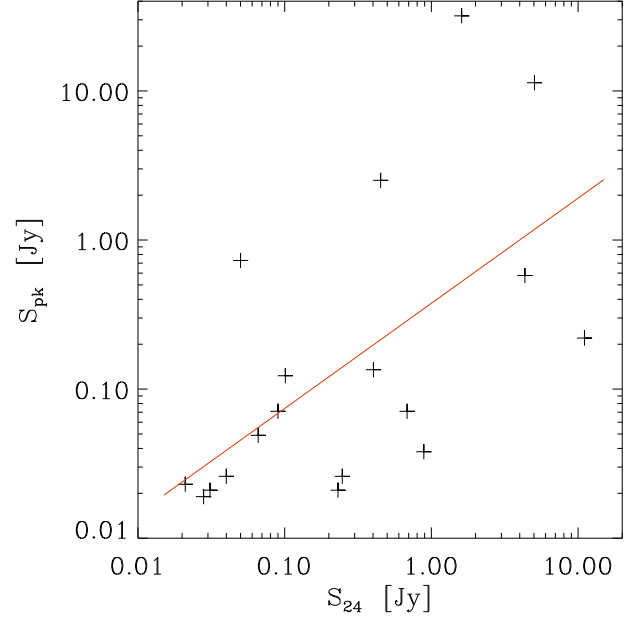


Fig. 12: Plot of the peak flux density of all methanol masers associated with a MIPS 24 μm counterpart vs. the flux density of the MIPS source. The solid line represents the linear fit to all points. The Spearman rank coefficient is 0.57.

the probability for the observer to be aligned with the beaming solid angle of one or more velocity components is clearly higher.

Variability of maser emission can be due to both regular and turbulent motions of material with different scales and lifetimes, besides to variations in the pumping source itself. In addition, maser condensations can split into separate fragments due to interaction with dense material of the medium where the masers are generated (see, e.g., Lekht et al. 2009). The overall evolution of the maser spots and their number is not known, but if the number of maser spots actually *increases* during the evolution of the star forming region, then our observations are consistent with these weak masers indeed representing an earlier stage.

5. Conclusions

We have observed 107 high-mass dust clumps with the Arecibo telescope in search for the 6.7-GHz methanol and 6.0-GHz excited OH masers. The clumps were selected from the Hi-GAL survey to be relatively massive and visible from Arecibo. We detected a total of 32 methanol masers, with 22 sources being new and weak (median peak flux density 0.07 Jy) detections, in the Galactic longitude range [32° 0, 59° 8].

We have compared our results with previous similar surveys, in particular with the ‘‘Arecibo Methanol Maser Galactic Plane Survey’’ (Pandian et al. 2007), and found that although both source samples approximately cover the same distance range,

our newly discovered masers are clearly shifted towards much lower integrated flux densities compared to the AMGPS. Using 5-pointings cross-scans we checked, in a sub-sample of sources, if the masers were being observed off-peak. In most cases, the resulting maser peak positions turned out to be very close (i.e., within the Arecibo pointing error) to the pointed positions, i.e. the nominal positions of the Hi-GAL sources. Thus, most of the methanol masers observed towards our Hi-GAL massive dust clumps appear to be intrinsically weaker compared to previously observed masers in unbiased surveys.

The reasons for this lower flux density have yet to be determined, and will likely need higher-angular resolutions observations. We found no statistically significant correlation with the physical parameters of the Hi-GAL clumps, except possibly for sources with both maser types which appear to have higher mass and luminosity compared to sources with just one type of maser emission. The merged luminosity function of the methanol masers detected by us and the AMGPS, shows an essentially flat distribution for luminosities between $\sim 10^{-7}$ and $\sim 10^{-5} L_{\odot}$ and a relatively quick drop outside of this range. The intensity of the methanol masers correlates well with the velocity range of the maser emission, which suggests that the low brightness of these masers is related to the number of maser spots in the emitting region and their evolution with time.

Acknowledgements. We wish to thank the staff of the Arecibo Observatory for the support provided before and during the observations. P.H. acknowledges support from NSF grant AST-0908901.

References

- Alcock, C. & Ross, R. R. 1985, *ApJ*, 290, 433
- Breen, S. L., Caswell, J. L., Ellingsen, S. P., & Phillips, C. J. 2010, *MNRAS*, 406, 1487
- Brunthaler, A., Reid, M. J., Menten, K. M., et al. 2011, *Astronomische Nachrichten*, 332, 461
- Caswell, J. L. & Vaile, R. A. 1995, *MNRAS*, 273, 328
- Caswell, J. L., Vaile, R. A., Ellingsen, S. P., Whiteoak, J. B., & Norris, R. P. 1995, *MNRAS*, 272, 96
- Charnley, S. B., Kress, M. E., Tielens, A. G. G. M., & Millar, T. J. 1995, *ApJ*, 448, 232
- Charnley, S. B., Tielens, A. G. G. M., & Millar, T. J. 1992, *ApJL*, 399, L71
- Cragg, D. M., Sobolev, A. M., & Godfrey, P. D. 2002, *MNRAS*, 331, 521
- Cragg, D. M., Sobolev, A. M., & Godfrey, P. D. 2005, *MNRAS*, 360, 533
- Cyganowski, C. J., Brogan, C. L., Hunter, T. R., & Churchwell, E. 2009, *ApJ*, 702, 1615
- Elia, D., Molinari, S., Fukui, Y., et al. 2013, *ApJ*, 772, 45
- Elia, D., Schisano, E., Molinari, S., et al. 2010, *A&A*, 518, L97
- Elitzur, M. 1992, *ARA&A*, 30, 75
- Ellingsen, S. P. 2006, *ApJ*, 638, 241
- Ellingsen, S. P., Breen, S. L., Sobolev, A. M., et al. 2011, *ApJ*, 742, 109
- Green, J. A., Caswell, J. L., Fuller, G. A., et al. 2009, *MNRAS*, 392, 783
- Green, J. A., Caswell, J. L., Fuller, G. A., et al. 2010, *MNRAS*, 409, 913
- Green, J. A., Caswell, J. L., Fuller, G. A., et al. 2008, *MNRAS*, 385, 948
- Green, J. A. & McClure-Griffiths, N. M. 2011, *MNRAS*, 417, 2500
- Hill, T., Burton, M. G., Minier, V., et al. 2005, *MNRAS*, 363, 405
- Hoare, M. G., Purcell, C. R., Churchwell, E. B., et al. 2012, *PASP*, 124, 939
- Jackson, J. M., Rathborne, J. M., Shah, R. Y., et al. 2006, *ApJS*, 163, 145
- Lekht, E. E., Silant'ev, N. A., & Alekseeva, G. A. 2009, *Astronomy Reports*, 53, 813
- Menten, K. M. 1991, *ApJL*, 380, L75
- Molinari, S., Swinyard, B., Bally, J., et al. 2010, *PASP*, 122, 314
- Olmi, L., Anglés-Alcázar, D., Elia, D., et al. 2013, *A&A*, 551, A111
- Pandian, J. D. & Goldsmith, P. F. 2007, *ApJ*, 669, 435
- Pandian, J. D., Goldsmith, P. F., & Deshpande, A. A. 2007, *ApJ*, 656, 255
- Pandian, J. D., Menten, K. M., & Goldsmith, P. F. 2009, *ApJ*, 706, 1609
- Pandian, J. D., Momjian, E., Xu, Y., Menten, K. M., & Goldsmith, P. F. 2011, *ApJ*, 730, 55
- Pestalozzi, M. 2012, in *IAU Symposium*, Vol. 287, *IAU Symposium*, ed. R. S. Booth, W. H. T. Vlemmings, & E. M. L. Humphreys, 492–496
- Pestalozzi, M., Humphreys, E. M. L., & Booth, R. S. 2002, *A&A*, 384, L15
- Pestalozzi, M. R., Chrysostomou, A., Collett, J. L., et al. 2007, *A&A*, 463, 1009
- Pestalozzi, M. R., Minier, V., & Booth, R. S. 2005, *A&A*, 432, 737
- Purcell, C. R., Hoare, M. G., Cotton, W. D., et al. 2013, *ApJS*, 205, 1
- Reach, W. T., Rho, J., & Jarrett, T. H. 2005, *ApJ*, 618, 297
- Reid, M. J., Menten, K. M., Zheng, X. W., et al. 2009, *ApJ*, 700, 137
- Russeil, D. 2003, *A&A*, 397, 133
- Russeil, D., Pestalozzi, M., Mottram, J. C., et al. 2011, *A&A*, 526, A151
- Schneider, N., Bontemps, S., Simon, R., et al. 2011, *A&A*, 529, A1
- Slysh, V. I., Val'tts, I. E., Kalenskii, S. V., et al. 1999, *A&AS*, 134, 115
- Szymczak, M. & Gérard, E. 2004, *A&A*, 414, 235
- Szymczak, M., Hrynek, G., & Kus, A. J. 2000, *A&AS*, 143, 269
- Szymczak, M., Kus, A. J., Hrynek, G., Kępa, A., & Pazderski, E. 2002, *A&A*, 392, 277
- van der Walt, J. 2005, *MNRAS*, 360, 153
- Walsh, A. J., Hyland, A. R., Robinson, G., & Burton, M. G. 1997, *MNRAS*, 291, 261

Appendix A: Spectra of methanol masers

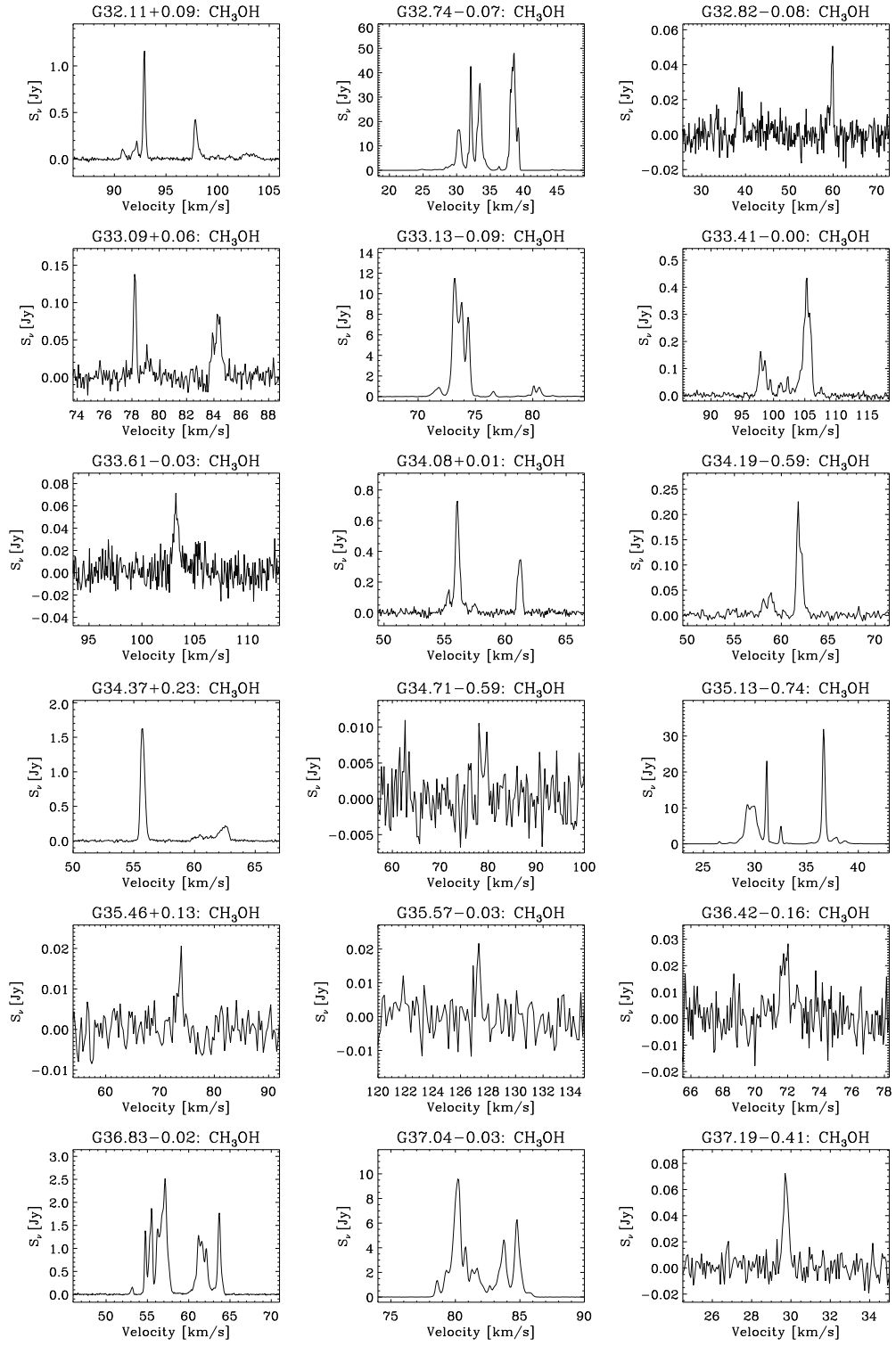


Fig. A.1: Spectra of methanol masers

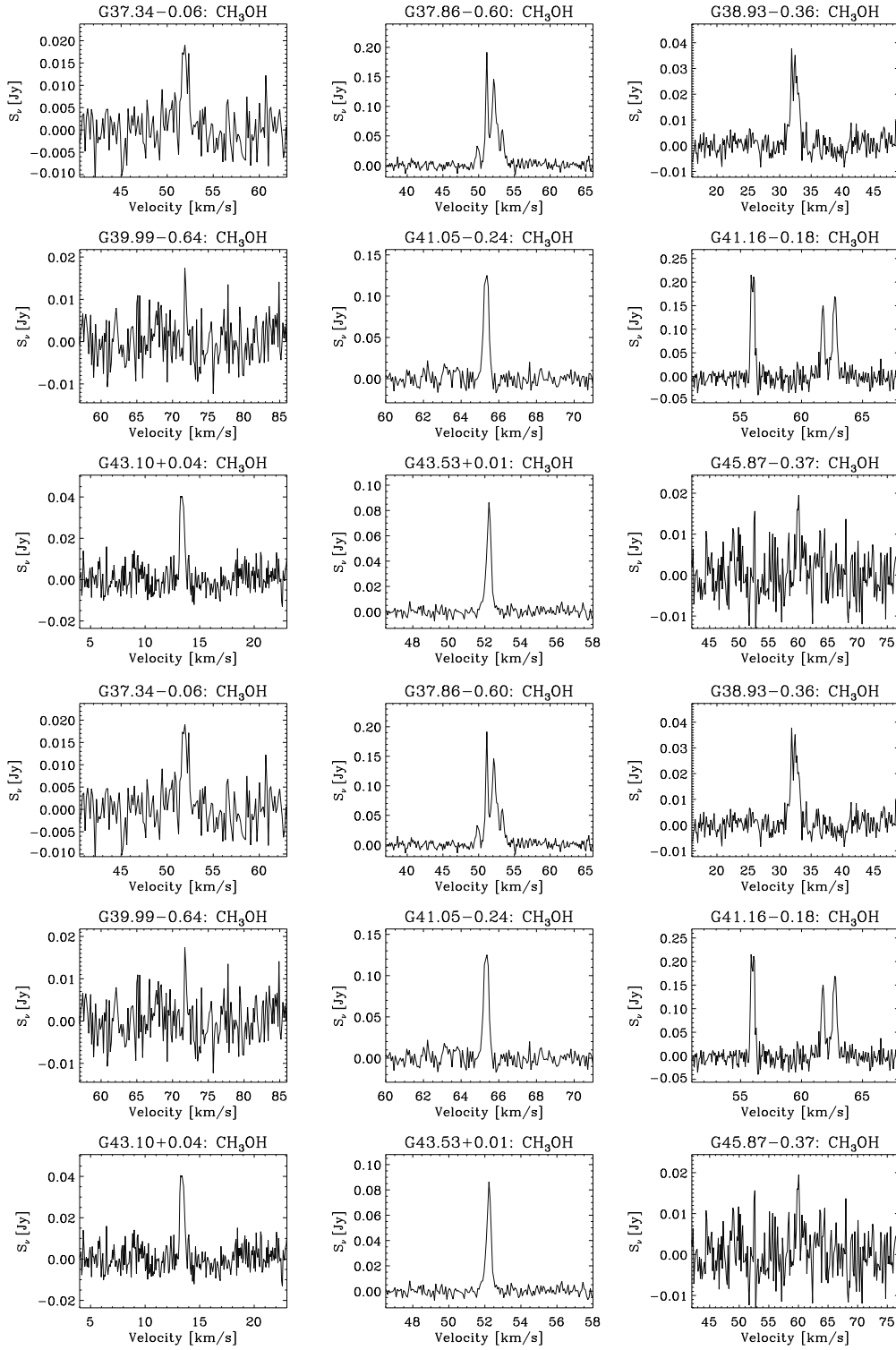


Fig. A.1: Continued.

Appendix B: Spectra of OH masers

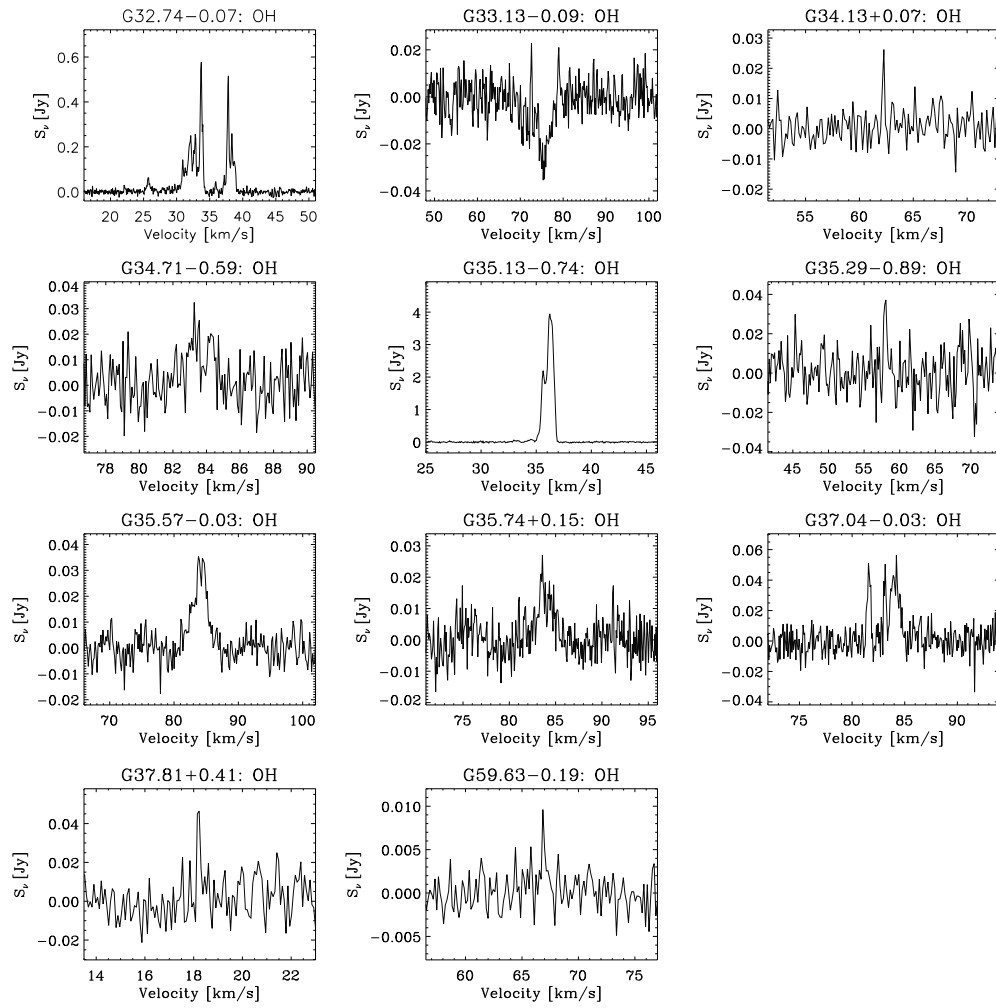


Fig. B.1: Spectra of OH masers

Appendix C: Sources with no methanol detection

Table C.1: Hi-GAL sources with no detection of 6.7-GHz methanol masers. The last column lists the RMS (in mJy) of the final spectrum.

Name	RA [J2000.0]	DEC [J2000.0]	RMS [mJy]
G32.45+0.38	18:49:11.6	-00:14:49.0	6
G32.45+0.15	18:50:00.2	-00:21:21.5	10
G32.03-0.32	18:50:58.1	-00:56:54.8	10
G33.11+0.06	18:51:33.3	00:11:43.1	10
G32.98-0.07	18:51:47.4	00:00:38.2	9
G33.26+0.06	18:51:48.4	00:19:37.9	10
G33.70+0.28	18:51:50.4	00:49:05.9	14
G33.71+0.25	18:51:57.1	00:48:48.6	9
G33.49-0.01	18:52:30.8	00:29:47.6	10
G33.02-0.36	18:52:54.6	-00:05:05.9	10
G34.46+0.24	18:53:20.5	01:28:26.0	9
G34.13+0.07	18:53:21.3	01:06:11.2	9
G33.33-0.53	18:54:03.9	00:06:55.4	9
G34.00-0.29	18:54:26.5	00:49:32.8	10
G35.42+0.43	18:54:27.2	02:24:52.7	9
G34.94+0.15	18:54:33.2	01:51:59.0	9
G34.69+0.00	18:54:39.2	01:34:22.0	9
G34.24-0.26	18:54:46.7	01:02:46.0	9
G34.93+0.01	18:55:01.1	01:47:23.5	9
G35.56+0.10	18:55:53.1	02:23:24.5	9
G35.60+0.10	18:55:56.1	02:25:58.3	9
G35.74+0.15	18:56:01.0	02:34:34.0	8
G35.44-0.00	18:56:03.1	02:13:49.1	10
G35.61-0.07	18:56:36.8	02:21:20.9	9
G35.68-0.17	18:57:04.9	02:21:59.0	8
G35.52-0.27	18:57:08.3	02:10:53.9	9
G36.40+0.02	18:57:42.0	03:06:07.9	9
G37.49+0.53	18:57:53.3	04:18:18.7	8
G36.45-0.18	18:58:31.4	03:03:01.5	9
G37.17+0.10	18:58:49.6	03:49:15.0	5
G37.61+0.31	18:58:51.5	04:18:33.6	11
G37.81+0.41	18:58:53.9	04:32:15.1	9
G35.29-0.89	18:58:57.0	01:41:40.0	18
G37.42+0.13	18:59:09.4	04:03:38.0	9
G37.37-0.23	19:00:23.7	03:50:38.9	9
G38.19-0.15	19:01:35.9	04:36:43.9	7
G38.42-0.16	19:02:04.6	04:48:24.6	8
G38.32-0.22	19:02:06.1	04:42:01.8	8
G39.25-0.05	19:03:12.8	05:35:51.2	10
G38.69-0.45	19:03:35.2	04:55:06.8	10
G38.92-0.41	19:03:52.9	05:08:12.9	7
G39.49-0.20	19:04:10.5	05:44:55.0	9
G38.35-0.95	19:04:44.8	04:23:18.9	8
G39.85-0.21	19:04:53.1	06:03:44.5	10
G39.26-0.58	19:05:07.9	05:22:00.0	8
G39.36-0.56	19:05:13.9	05:27:34.1	8
G40.36-0.05	19:05:15.7	06:34:52.3	8
G39.99-0.64	19:06:39.9	05:59:13.7	9
G43.23-0.04	19:10:33.5	09:08:25.0	8
G42.15-0.66	19:10:45.5	07:53:43.8	9
G43.51+0.01	19:10:51.6	09:25:01.3	9
G42.23-0.65	19:10:53.3	07:58:23.6	9
G43.30-0.21	19:11:16.9	09:07:29.7	8
G43.32-0.20	19:11:17.4	09:08:48.8	8
G44.48-0.13	19:13:12.9	10:12:20.9	10
G44.49-0.15	19:13:17.5	10:12:08.8	10
G45.95+0.07	19:15:14.4	11:36:17.6	9
G47.04+0.25	19:16:41.5	12:39:19.9	10

G47.09-0.27	19:16:42.2	12:42:27.0	7
G45.38-0.74	19:17:07.5	10:43:09.6	10
G45.88-0.51	19:17:14.0	11:16:18.9	7
G46.42-0.23	19:17:16.8	11:52:31.0	8
G46.17-0.52	19:17:49.1	11:31:03.7	4
G47.00-0.26	19:18:28.6	12:22:36.8	5
G54.45+1.01	19:28:25.8	19:32:33.5	7
G54.39+0.92	19:28:38.0	19:26:51.9	7
G54.11-0.08	19:31:48.7	18:42:58.0	7
G54.22-0.11	19:32:10.6	18:47:52.9	7
G55.74+0.11	19:34:27.2	20:14:33.1	8
G55.15-0.29	19:34:45.9	19:31:39.4	5
G56.06-0.12	19:36:00.0	20:24:08.7	7
G56.89-0.18	19:37:58.4	21:05:55.6	9
